NANO LETTERS

pubs.acs.org/NanoLett

Letter

Current−Phase Relation of a WTe_2 Josephson Junction

Martin Endres,* Artem Kononov, Hasitha Suriya Arachchige, Jiaqiang Yan, David Mandrus, Kenji Watanabe, Takashi Taniguchi, and Christian Schönenberger

Cite This: Nano Lett. 2023, 23, 4654−4659

Read Online

ACCESS | Metrics & More | Article Recommendations | Supporting Information

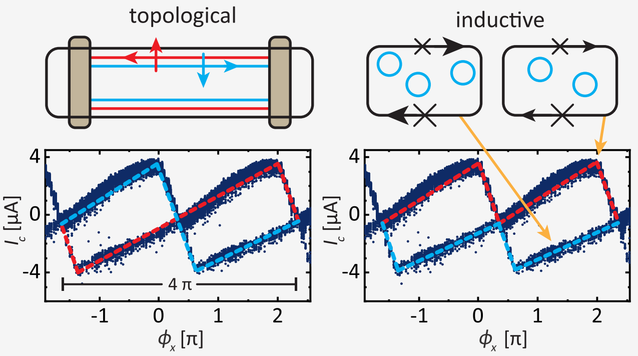

ABSTRACT: When a topological insulator is incorporated into a Josephson junction, the system is predicted to reveal the fractional Josephson effect with a 4π-periodic current−phase relation. Here, we report the measurement of a 4π-periodic switching current through an asymmetric SQUID, formed by the higher-order topological insulator WTe_2. Contrary to the established opinion, we show that a high asymmetry in critical current and negligible loop inductance are not sufficient by themselves to reliably measure the current−phase relation. Instead, we find that our measurement is heavily influenced by additional inductances originating from the self-formed $PdTe_x$ inside the junction. We therefore develop a method to numerically recover the current−phase relation of the system and find the 1.5 μm long junction to be best described in the short ballistic limit. Our results highlight the complexity of subtle inductance effects that can give rise to misleading topological signatures in transport measurements.

KEYWORDS: *WTe_2, topological superconductivity, higher-order topological insulators, edge states, current−phase relation, asymmetric SQUID*

Topological insulators (TIs) belong to a unique class of materials that are insulating in their bulk while hosting gapless boundary states that are protected by time-reversal symmetry.[1] The class of three-dimensional TIs has recently been extended,[2,3] realizing that a d-dimensional TI of order n can develop $(d - n)$-dimensional hinge or corner states. A promising candidate of this novel material class that is predicted to host topological hinge states is the semimetallic transition-metal dichalcogenide WTe_2.[4−7] While bulk states dominate transport in the normal state, hinge states become the governing transport channel over long distances in the superconducting state, as they can carry a higher critical current due to their reduced dimensionality.[8,9] Therefore, Josephson junctions (JJs) formed by a TI as the weak link between two superconducting electrodes provide an ideal platform to probe the topological nature in a transport experiment. Topological hybrid systems are of great interest, as they are predicted to host unconventional superconductivity,[10] the fundamental building block of a potential topologically protected quantum bit.[11] The fingerprint of a JJ is the current−phase relation (CPR), the dependence of the supercurrent on the phase difference φ between the superconducting electrodes. The measurement of the CPR directly reflects the underlying transport mechanism with which the Cooper pairs are shuttled across the weak link. For a topological weak link, perfect Andreev reflection is expected,[12] since spin-momentum locking in the hinge states prohibits normal electron reflection at the interface to the superconductor. In the long junction limit, the supercurrent is carried by 4π-periodic Andreev bound states of opposite parity, σ^+ and σ^-, that give rise to a characteristic sawtooth-shaped I_c. Parity conservation prohibits the recombination to the lower energy branch and results in a multivalued I_c with a distinct diamond shape, as plotted in Figure 1a.[13] For comparison, the expected CPR of a trivial ballistic JJ in the long junction limit is plotted as a black dashed line in the same figure. Accordingly, the literature often infers ballistic topological states from the observation of a sawtooth-shaped flux dependence of the critical current.[9,14−16]

Recently, high-quality JJs formed in WTe_2 on palladium (Pd) bottom contacts have been reported[17,18] and provided evidence of a nonsinusoidal CPR.[7,19] Here, we combine such JJs based on Pd-induced superconductivity in WTe_2 with external superconducting leads, as illustrated in Figure 1b. A superconducting quantum interference device (SQUID) formed out of two such JJs is expected to reflect the CPR, provided that the critical current amplitudes of the two JJs are

Received: April 14, 2023
Revised: May 2, 2023
Published: May 8, 2023

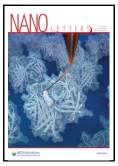

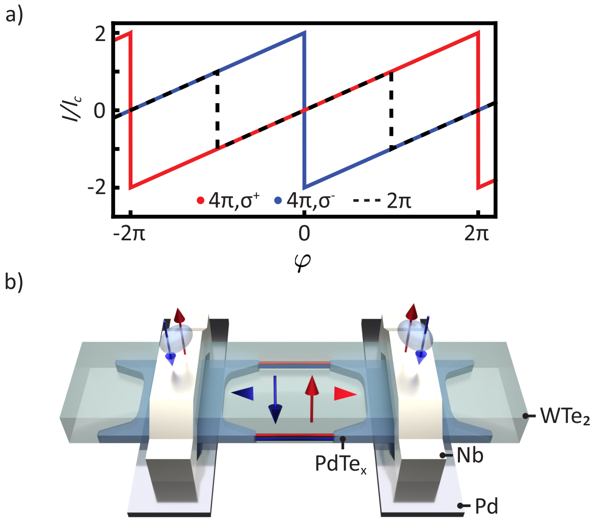

Figure 1. CPR of a topological JJ. (a) Normalized CPR of a topological JJ in the long junction limit as a function of the junction phase φ. The 4π-periodic supercurrent through the SQUID is carried by Andreev bound states of opposite parity, σ^+ and σ^-, resulting in a multivalued switching current that resembles a diamond-like pattern. A 2π-periodic CPR of a topologically trivial junction is shown as a dashed line for comparison. (b) llustration of a JJ fabricated from an elongated WTe_2 crystal on top of Pd bottom contacts. Superconducting Nb contacts were deposited from above after etching through the top hBN (not displayed). The diffusion of Pd into the WTe_2 crystal leads to the formation of superconducting $PdTe_x$ inside the weak link, through which the topological hinge states can be coupled.

highly different and the loop inductance is negligible.[20,21] Based on this method, we observe a switching current distribution with 4π-periodicity that resembles a topological JJ.[13] Contrary to the topological interpretation, we provide an alternative explanation based on inductance effects,[22] which could be relevant for a number of previous experiments.[9,14−16] Importantly, the inductance contribution originates from the JJs themselves and exceeds the loop inductance. We further developed a numerical model based on the maximization of the supercurrent in the SQUID loop that allows us to exclude screening effects from the additional inductances and recover the real CPR. The calculations suggest that the critical current of our 1.5 μm long junction is best reproduced in the short ballistic limit, despite its long physical length.

We begin with the fabrication of an asymmetric SQUID out of WTe_2. In our experiment, both JJs are formed in the same needle-shaped WTe_2 flake of width w = 1.5 μm. The asymmetry in critical current I_c of the two involved JJs is achieved by a different spacing between the Pd bottom contacts l_w = 1.5 μm and l_r = 0.5 μm for the weak and reference junction, respectively, as sketched in Figure 2a. The superconducting loop is formed by etching through the top hBN into WTe_2 and sputtering niobium (Nb) on top. The Nb leads are between 2.2 and 3 μm wide and 100 nm thick. A detailed description of the fabrication process can be found in the Supporting Information. Figure 2a displays an optical image of the finished devices. In the following we will focus on the lower SQUID, enclosed by the dashed line.

The critical current of the SQUID is given by the sum $I_c(\varphi_w, \varphi_r) = I_c^w f_w(\varphi_w) + I_c^r f_r(\varphi_r)$ of the individual currents I_w and I_r through the two branches of the loop, defined by the critical current I_c^i and the normalized CPR f_i of the ith Josephson junction. The total flux Φ_{tot} threading the loop connects the phase differences across the two JJs $\varphi_w - \varphi_r = 2\pi\Phi_{tot}/\Phi_0 = \phi_{tot}$, with ϕ_{tot} denoting the external phase. In the absence of inductances in the loop, ϕ_{tot} is simply defined by the external phase ϕ_x. The asymmetry $I_c^r \gg I_c^w$ pins $\varphi_r = \varphi_r^{max}$ at a fixed phase, for which I_c^r is maximized.[20,21,23] The normalized CPR of the weak junction f_w can then be deduced from the measurement of

$$I_c(\phi_x) \approx I_c^w f_w(\varphi_r^{max} + \phi_x) + I_c^r f_r(\varphi_r^{max}) \tag{1}$$

In the experiment, $\Phi_x = BA_o$ is controlled by an applied perpendicular magnetic field B threading the effective loop area A_o = 186 μm^2. The Meissner screening of the enclosing superconducting loop was taken into account by including half of its width into the loop area. The final device is probed in a quasi four-terminal configuration by sourcing an ac current and monitoring the voltage drop over the SQUID. We use the counter technique, as described in the Supporting Information, to measure the switching statistics of the device.

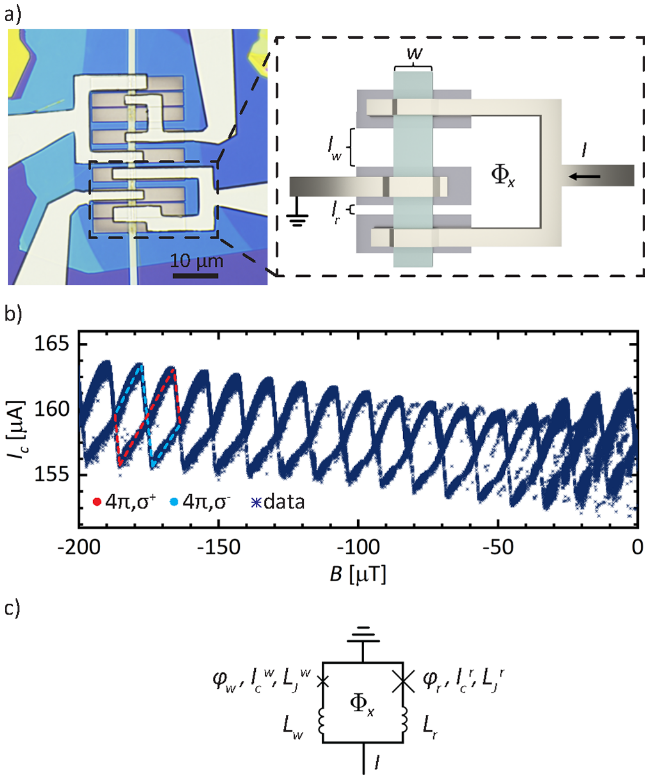

Figure 2. Switching statistics of the weak junction in an asymmetric SQUID. (a) Optical image of a SQUID device on the left, with the measured SQUID highlighted by the dashed box. An illustration of the device parameters is provided to the right. (b) High-resolution measurement of the SQUID switching current as a function of applied magnetic field through the loop. Oscillation periods of the parity states σ^+ and σ^-, respectively, are highlighted in red and light blue, respectively. The period δB = 23.2 μT of a single parity branch displays a 4π-periodicity with respect to the designed loop area δB = 11.1 μT. (c) Schematic of the SQUID, specifying the device parameters, including the additional series inductances L_w and L_r in series to the weak and reference JJ, respectively.

Figure 2b presents the measured switching statistics of the SQUID in an extended magnetic field range at base temperature T = 30 mK of the cryostat. Visible is a multivalued

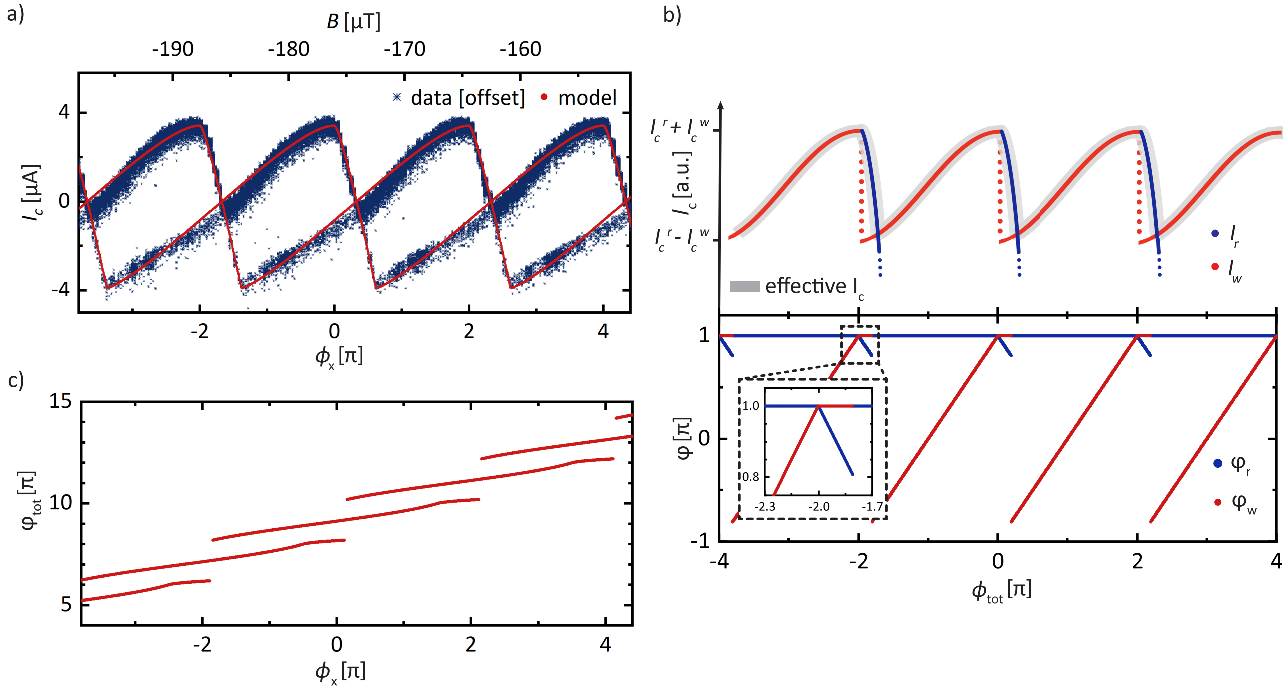

Figure 3. SQUID oscillations and numerical model of the CPR. (a) Experimental data of the SQUID oscillations as a function of external flux ϕ_x shown in blue. The red data points are a fit to the data based on maximizing the critical current in the SQUID loop. Phase winding in the superconducting loop is responsible for the multivalued supercurrent. (b) Visual method to maximize I_c as a function of total flux ϕ_{tot}. The upper panel plots the currents I_r and I_w for a short ballistic CPR with an amplitude ratio $I_c^r/I_c^w = 40$. The two currents evolve in opposite directions with increasing ϕ_{tot}, due to $\varphi_r - \varphi_w = \phi_{tot}$. The resulting maximized I_c is highlighted by a gray background and is composed of the weak junction and the reference junction CPR for the rising and falling sides, respectively. The lower panel shows the corresponding behavior of the junction phases φ_r and φ_w, obtained through the numerical maximization model. The phases are mapped to the range of the CPR. The switch between the observed weak and reference junction branch in the top panel is accompanied by a shift from a fixed φ_r to φ_w at flux values of multiples of 2π. (c) Numerically calculated ϕ_{tot} versus ϕ_x using the model described in the main text. Inductance effects give rise to the multivalued $\phi_x(\phi_{tot})$, responsible for the intertwined branches visible in (a).

I_c that oscillates periodically around the offset current $I_c^r = 160$ μA of the reference junction. Given the great difference in critical current amplitudes $I_c^r/I_c^w \approx 40$, we expect the SQUID to be highly asymmetric and the measured signal to reflect the CPR of the weak JJ. A second set of oscillations appears for field values from $B = -100$ μT upward and is explained in the Supporting Information by the behavior of the reference junction. The extracted oscillation period of a fixed parity branch, as defined in Figure 1a, is equal to $\delta B = 23.2$ μT and therefore twice the value $\delta B = \Phi_0/A_o = 11.1$ μT expected for the enclosed loop area A_o. The data represent striking resemblance to the two parity states of a topological JJ in the long junction limit with a 4π-periodicity in flux. However, the amplitude of the signal deems this explanation unlikely. A single channel in the topological ballistic long junction can carry a current $I_{c,4\pi} = E_{Th}e/\hbar = v_F e/l$,[13] with E_{Th} being the Thouless energy, v_F the Fermi velocity, and l the length of the weak link. I_c in our junction would therefore have to be carried by at least $I_c^w l_w/(ev_F) \approx 116$ perfectly ballistic channels in parallel, assuming $v_F = 3.09 \times 10^5$ m s^{-1}.[24] WTe$_2$ is expected to host a pair of hinge states on opposite edges of the crystal.[19] Conducting states have been found to reside at step edges in the crystal where the number of vdW layers changes,[7] but we do not observe such crystal steps in optical microscopy for the used flake. We conclude that it is unlikely for the current to be carried purely by ballistic hinge states.

Instead, multivalued CPR measurements have previously been reported in devices containing a superconducting weak link with large kinetic inductance that is responsible for strong screening effects.[22,25−28] In strong contrast to previous experiments, however, the device studied here contains a normal conducting weak link[18] and has negligible loop inductance, as will be shown later.

The schematic in Figure 2c introduces a set of additional inductances, L_r and L_w, that are placed in series to the reference and weak junction, respectively, while potential mutual inductances are assumed to be negligible. In general, the total phase

$$\phi_{tot} = \phi_x + 2\pi(L_r I_r - L_w I_w)/\Phi_0 \tag{2}$$

can differ strongly from the phase created by the external flux $\phi_x = 2\pi\Phi_x/\Phi_0$, due to the contribution induced by the currents I_r and I_w passing through the inductances in the SQUID arms, L_r and L_w. We note that while a screening current can distort the flux dependence of the critical current, it does not change its periodicity.[29]

Deducing the CPR from the inductive SQUID measurement requires the knowledge of the phase dependences of $I_r(\phi_{tot})$ and $I_w(\phi_{tot})$ themselves. In order to bypass this recursive constraint, we make an assumption about the CPRs of the JJs that is based on the experimental data. We are then going to use this information in the next step to calculate $\phi_r^{max}(\varphi_{tot})$, for which $I_c(\phi_{tot})$ is maximized according to eq 1. Last, we are going to include screening effects in the model and obtain the relation $I_c(\phi_x)$, which is placed in context to the experimental data.

Our choice of CPR for the weak junction is based on two experimental observations. First, the rising slope of $I_c(\phi_x)$ is nonlinear, suggesting the same should hold for the CPR. Second, $I_c(\phi_x)$ has self-crossings, implying that the phase of the reference junction does not remain fixed, contrary to the established expectation for a highly asymmetric SQUID. The behavior is possible if the CPR of the weak junction contains abrupt changes, such as is the case in the ballistic limit of the CPR. We illustrate this behavior later in the text and provide an additional discussion in the Supporting Information. $I_w(\varphi_w)$ is modeled to be in the 2π-periodic, ballistic short junction limit[30]

$$I_w(\varphi_w) = I_c^w \frac{\sin\varphi_w}{\sqrt{1-\sin^2(\varphi_w/2)}} \tag{3}$$

scaled by the amplitude of I_c^w. The exact CPR of the reference junction plays little role in the further discussion, yet, since it is formed in the same material but with reduced length, we also model it as a short ballistic junction, scaled by I_c^r. Independently, we have used length-dependent measurements in the Supporting Information and the analysis of the $PdTe_x$ diffusion profile in ref 18 to verify that both junctions behave indeed as JJs and are not shorted by $PdTe_x$.[31]

Having made this initial assumption, we continue to calculate the resulting I_c by maximizing the current through the SQUID. The top panel in Figure 3b illustrates a visual method to maximize the critical current as a function of ϕ_{tot}. The individual currents through the SQUID arms I_r and I_w follow eq 3. The currents evolve in opposite flux direction, due to the connection $\varphi_r - \varphi_w = \phi_{tot}$. We start at the configuration $\phi_r = \phi_r^{max}$ and $\phi_w = \phi_w^{max}$, when the currents through the reference and weak junctions are at their maximum, I_c^r and I_c^w, respectively. Moving from this point in the negative direction of ϕ_{tot}, I_c follows I_w, plotted as a red curve. In the opposite direction toward positive values of ϕ_{tot}, I_w faces a sudden drop. Instead of following I_w, a higher I_c is obtained by following I_r, drawn in dark blue, until the point when I_r intersects with I_w. This creates a small flux range $\delta\varphi_{tot} \propto \pi I_c^w/I_c^r \ll \pi$, in which I_c is maximized by following I_r rather than I_w, resulting in a changing φ_r, while $\phi_w^{max} = \pi$ remains fixed. The situation is illustrated in the lower panel of Figure 3b. Once the two current branches cross with evolving flux, φ_r returns to its maximum value $\phi_r^{max} = \pi$ and $I_c(\phi_{tot})$ follows the flux dependence of I_w. The well-known behavior of the asymmetric SQUID is restored. While $\delta\phi_{tot}$ remains small in the above scenario, it can extend significantly in the experiment, due to the inductance effects, as described by eq 2.

Given that φ_r does not necessarily remain fixed in an asymmetric SQUID, we introduce next a numerical procedure to transfer the above model from the dependence of total flux ϕ_{tot} to the external flux ϕ_x, the quantity applied in the experiment. The slope of $I_c(\phi_x)$ is directly related to the inductance of the current carrying arm in the SQUID, via $\mathrm{d}I_c/\mathrm{d}\varphi_x = \Phi_0/(2\pi(L_i + L_J^i))$, with L_J^i being the Josephson inductance and i = r, w, depending on the considered data mapping the CPR of the reference or the weak junction.

First, we numerically maximize the expression

$$I_c(\phi_{tot}) = \max_{\varphi_r}\{I_r(\varphi_r(\phi_{tot})) + I_w(\varphi_r(\phi_{tot}) + \phi_{tot})\} \tag{4}$$

with respect to $\varphi_r(\phi_{tot})$ for a given ϕ_{tot}. I_r and I_w correspond to the currents through the respective SQUID arms, i.e. $I_r = I_c^r f(\phi_r)$ and $I_w = I_c^w f(\phi_r + \varphi_{tot})$. The two amplitudes $I_c^r = 160\ \mu A$ and $I_c^w = 3.75\ \mu A$ are determined from the fixed current background and the oscillation amplitude of the intertwined branches. The lower panel in Figure 3b plots the obtained φ_r and φ_w in blue and red, respectively. Based on the choice of the CPR function in eq 3, φ_r is mostly fixed at the maximum value $\phi_r^{max} = \pi$, while φ_w evolves linearly in ϕ_{tot}, according to $\phi_w = \varphi_{tot} + \phi_r^{max}$. However, a small range $\delta\phi_{tot}$ exists, where φ_r changes in flux while φ_w remains fixed, in agreement with the graphical method introduce above in the upper panel of Figure 3b.

Using $\varphi_r(\phi_{tot})$, it is now possible to extract the inductance effects and recalculate $\phi_x = \phi_{tot} - 2\pi(L_r I_r - L_w I_w)/\Phi_0$. Depending on the magnitude of the incorporated inductances and critical currents, self-inductance effects in the loop cause the connection $\phi_{tot}(\phi_x)$ to become multivalued, as is visible from Figure 3c.

Finally, $I_c(\phi_x)$ is plotted in red in Figure 3a. Despite the long physical length $L_w = 1.5\ \mu m$ of the junction, we find the bending of the gradually rising slope $\mathrm{d}I_c/\mathrm{d}\phi_x$ to be well reproduced by f_w being in the 2π-periodic, ballistic short junction limit. In both cases, the magnetic field dependences of the current amplitudes are assumed to be negligible for the given field range. Importantly, despite the great difference in critical current amplitudes of the embedded junctions, the model confirms that φ_r does not remain fixed in flux. The experimental CPR of the SQUID is composed of the weak and the reference junction CPR. Even though the CPR of the weak junction is not necessarily uniquely in the short junction limit, it has to have a sharp transition in flux and therefore be close to ballistic in order to ease the shift between the fixed φ_r and φ_w.

Further, we extract the inductances $L_r = 60$ pH and $L_w = 220$ pH, by matching the rising and falling slopes of the fit to the data. An important result that distinguishes ours from previous experiments is that L_r and L_w by themselves exceed the sum of geometrical inductance $L_{geo} \approx 27.0$ pH[32] and kinetic inductance $L_{kin} \approx 5.5$ pH[33] for the Nb SQUID loop. Possibly, additional JJs can form at the interface between the sputtered superconducting leads and the self-formed superconducting $PdTe_x$,[34] yet given that their critical current has to be larger than I_c^r, little inductance contribution is to be expected. Instead, we attribute the origin of additional inductance and its asymmetry between the SQUID arms to the superconducting $PdTe_x$ that has self-formed at the interface between WTe_2 and Pd. Further support of this interpretation is provided in the Supporting Information, including the comparison of the data to different initial CPR assumptions.

Finally, the multivalued I_c can also be explained in the framework of excited vorticity states in an inductive SQUID.[25−28,35] Using the parameters obtained from our fit, we calculate the magnetic screening factor $\beta_L = \pi I_c^w(L_w + L_r)/\Phi_0 > 1$,[29] reflecting that an additional flux quantum can be created by the maximum circulating current through the weak JJ. The result is a multivalued ϕ_{tot} as a function of ϕ_x, as was shown in Figure 3c for the given device parameters. The above behavior can differ strongly even on a single sample chip. While the second SQUID loop formed on the same WTe_2 flake (compare Figure 2a) reveals the same behavior of the reference junction with multiple branches, we do not observe higher-vorticity states in the SQUID oscillations. The absence of the feature is most likely connected to the overall smaller I_c^w, despite the shorter junction length with $l_w = 1.2\ \mu$m.

In conclusion, the established assumption of a fixed reference junction phase in flux does not hold for highly transparent junctions, even in the case of highly asymmetric critical current amplitudes. Furthermore, we have shown the complexity of subtle inductance effects that reach beyond the standard consideration of the loop inductance and might create misleading topological features. It is therefore crucial for a correct CPR measurement to consider potential inductance contributions from the interfaces between the embedded junctions with the SQUID loop. The origin of such additional inductances can go beyond the diffusion of $PdTe_x$ presented here and may include defects implanted at the interface through various fabrication steps.[33,36] Despite these limitations, the fitting routine presented here allows reproduction of the experimental data closely. The best result was obtained by placing the weak junction in the short ballistic limit, as presented in the Supporting Information. Our results establish WTe_2 as a promising platform for further experiments toward topological superconductivity.

■ ASSOCIATED CONTENT

Data Availability Statement

All data in this publication are available in numerical form in the Zenodo repository.[37]

SI Supporting Information

The Supporting Information is available free of charge at https://pubs.acs.org/doi/10.1021/acs.nanolett.3c01416.

> Materials and methods, counter measurement technique, inductance effects in single Josephson junctions, verification of the inductance effects, comparison of the CPR configurations in the fitting procedure, instability of the reference junction phase φ_r, and frequency dependence of the switching statistics (PDF)

■ AUTHOR INFORMATION

Corresponding Author

Martin Endres − *Department of Physics, University of Basel, 4056 Basel, Switzerland;* orcid.org/0000-0001-7749-3585; Email: martin.endres@unibas.ch

Authors

Artem Kononov − *Department of Physics, University of Basel, 4056 Basel, Switzerland;* orcid.org/0000-0002-3778-8239

Hasitha Suriya Arachchige − *Department of Physics and Astronomy, University of Tennessee, Knoxville, Tennessee 37996, United States*

Jiaqiang Yan − *Department of Physics and Astronomy, University of Tennessee, Knoxville, Tennessee 37996, United States; Material Science and Technology Division, Oak Ridge Laboratory, Oak Ridge, Tennessee 37831, United States;* orcid.org/0000-0001-6625-4706

David Mandrus − *Department of Materials Science and Engineering, University of Tennessee, Knoxville, Tennessee 37996, United States; Department of Physics and Astronomy, University of Tennessee, Knoxville, Tennessee 37996, United States; Material Science and Technology Division, Oak Ridge Laboratory, Oak Ridge, Tennessee 37831, United States;* orcid.org/0000-0003-3616-7104

Kenji Watanabe − *Research Center for Functional Materials, National Institute for Materials Science, Tsukuba 305-0044, Japan;* orcid.org/0000-0003-3701-8119

Takashi Taniguchi − *International Center for Materials Nanoarchitectonics, National Institute for Materials Science, Tsukuba 305-0044, Japan;* orcid.org/0000-0002-1467-3105

Christian Schönenberger − *Department of Physics, University of Basel, 4056 Basel, Switzerland; Swiss Nanoscience Institute, University of Basel, 4056 Basel, Switzerland;* orcid.org/0000-0002-5652-460X

Complete contact information is available at: https://pubs.acs.org/10.1021/acs.nanolett.3c01416

Author Contributions

M.E. and A.K. contributed equally.

Author Contributions

M.E. fabricated the devices. M.E. and A.K. measured the devices. H.S.A., J.Y., and D.M. provided the WTe_2 crystals. K.W. and T.T. provided the hBN crystals. M.E., A.K., and C.S. analyzed the data and wrote the manuscript.

Notes

Similar experimental results have been obtained recently in ref 16; however, the authors provide a different interpretation.
The authors declare no competing financial interest.

■ ACKNOWLEDGMENTS

This project has received funding from the European Research Council (ERC) under the European Union's Horizon 2020 research and innovation programme: grant agreement No. 787414 TopSupra, by the Swiss National Science Foundation through the National Centre of Competence in Research Quantum Science and Technology (QSIT), and by the Swiss Nanoscience Institute (SNI). A.K. was supported by the Georg H. Endress foundation. D.M. and J.Y. acknowledge support from the U.S. Department of Energy (U.S.-DOE), Office of Science-Basic Energy Sciences (BES), Materials Sciences and Engineering Division. H.S.A. was supported by the Gordon and Betty Moore Foundation's EPiQS Initiative through Grant GBMF9069 and the Shull Wollan Center Graduate Research Fellowship. D.M. acknowledges support from the Gordon and Betty Moore Foundation's EPiQS Initiative, Grant GBMF9069. K.W. and T.T. acknowledge support from the Elemental Strategy Initiative conducted by MEXT, Japan and the CREST (JPMJCR15F3), JST and from the JSPS KAKENHI (Grant Numbers 19H05790 and 20H00354).

■ REFERENCES

(1) Fu, L.; Kane, C. L. Topological insulators with inversion symmetry. *Phys. Rev. B* **2007**, *76*, 045302.

(2) Schindler, F.; Cook, A. M.; Vergniory, M. G.; Wang, Z.; Parkin, S. S.; Bernevig, B. A.; Neupert, T. Higher-order topological insulators. *Science Advances* **2018**, *4*, No. eaat0346.

(3) Benalcazar, W. A.; Bernevig, B. A.; Hughes, T. L. Quantized electric multipole insulators. *Science* **2017**, *357*, 61.

(4) Wang, Z.; Wieder, B. J.; Li, J.; Yan, B.; Bernevig, B. A. Higher-Order Topology, Monopole Nodal Lines, and the Origin of Large Fermi Arcs in Transition Metal Dichalcogenides XTe_2 (X = Mo, W). *Phys. Rev. Lett.* **2019**, *123*, 186401.

(5) Peng, L.; Yuan, Y.; Li, G.; Yang, X.; Xian, J.-J.; Yi, C.-J.; Shi, Y.-G.; Fu, Y.-S. Observation of topological states residing at step edges of WTe_2. *Nat. Commun.* **2017**, *8*, 1.

(6) Huang, C.; Narayan, A.; Zhang, E.; Xie, X.; Ai, L.; Liu, S.; Yi, C.; Shi, Y.; Sanvito, S.; Xiu, F. Edge superconductivity in multilayer WTe_2 Josephson junction. *National Science Review* **2020**, *7*, 1468.

(7) Kononov, A.; Abulizi, G.; Qu, K.; Yan, J.; Mandrus, D.; Watanabe, K.; Taniguchi, T.; Schönenberger, C. One-dimensional edge transport in few-layer WTe_2. *Nano Lett.* **2020**, *20*, 4228.

(8) Heikkilä, T. T.; Särkkä, J.; Wilhelm, F. K. Supercurrent-carrying density of states in diffusive mesoscopic josephson weak links. *Phys. Rev. B* **2002**, *66*, 184513.

(9) Murani, A.; Kasumov, A.; Sengupta, S.; Kasumov, Y. A.; Volkov, V.; Khodos, I.; Brisset, F.; Delagrange, R.; Chepelianskii, A.; Deblock, R.; Bouchiat, H.; Guéron, S. Ballistic edge states in bismuth nanowires revealed by squid interferometry. *Nat. Commun.* **2017**, *8*, 1.

(10) Fu, L.; Kane, C. L. Superconducting proximity effect and majorana fermions at the surface of a topological insulator. *Phys. Rev. Lett.* **2008**, *100*, 096407.

(11) Hyart, T.; van Heck, B.; Fulga, I. C.; Burrello, M.; Akhmerov, A. R.; Beenakker, C. W. J. Flux-controlled quantum computation with majorana fermions. *Phys. Rev. B* **2013**, *88*, 035121.

(12) Adroguer, P.; Grenier, C.; Carpentier, D.; Cayssol, J.; Degiovanni, P.; Orignac, E. Probing the helical edge states of a topological insulator by cooper-pair injection. *Phys. Rev. B* **2010**, *82*, 081303.

(13) Beenakker, C. W. J.; Pikulin, D. I.; Hyart, T.; Schomerus, H.; Dahlhaus, J. P. Fermion-Parity Anomaly of the Critical Supercurrent in the Quantum Spin-Hall Effect. *Phys. Rev. Lett.* **2013**, *110*, 017003.

(14) Kayyalha, M.; Kazakov, A.; Miotkowski, I.; Khlebnikov, S.; Rokhinson, L. P.; Chen, Y. P. Highly skewed current−phase relation in superconductor−topological insulator−superconductor Josephson junctions. *npj Quantum Materials* **2020**, *5*, 7.

(15) Li, C.; De Ronde, B.; De Boer, J.; Ridderbos, J.; Zwanenburg, F.; Huang, Y.; Golubov, A.; Brinkman, A. Zeeman-effect-induced 0-π transitions in ballistic Dirac semimetal Josephson junctions. *Physical review letters* **2019**, *123*, 026802.

(16) Bernard, A.; Peng, Y.; Kasumov, A.; Deblock, R.; Ferrier, M.; Fortuna, F.; Volkov, V.; Kasumov, Y. A.; Oreg, Y.; von Oppen, F.; et al. Long-lived Andreev states as evidence for protected hinge modes in a bismuth nanoring Josephson junction. *Nat. Phys.* **2023**, *19*, 358.

(17) Kononov, A.; Endres, M.; Abulizi, G.; Qu, K.; Yan, J.; Mandrus, D. G.; Watanabe, K.; Taniguchi, T.; Schönenberger, C. Superconductivity in type-II Weyl-semimetal WTe_2 induced by a normal metal contact. *J. Appl. Phys.* **2021**, *129*, 113903.

(18) Endres, M.; Kononov, A.; Stiefel, M.; Wyss, M.; Arachchige, H. S.; Yan, J.; Mandrus, D.; Watanabe, K.; Taniguchi, T.; Schönenberger, C. Transparent Josephson junctions in higher-order topological insulator WTe_2 via Pd diffusion. *Phys. Rev. Materials* **2022**, *6*, L081201.

(19) Choi, Y.-B.; Xie, Y.; Chen, C.-Z.; Park, J.; Song, S.-B.; Yoon, J.; Kim, B. J.; Taniguchi, T.; Watanabe, K.; Kim, J.; et al. Evidence of higher-order topology in multilayer WTe_2 from Josephson coupling through anisotropic hinge states. *Nat. Mater.* **2020**, *19*, 974.

(20) Della Rocca, M. L.; Chauvin, M.; Huard, B.; Pothier, H.; Esteve, D.; Urbina, C. Measurement of the Current-Phase Relation of Superconducting Atomic Contacts. *Phys. Rev. Lett.* **2007**, *99*, 127005.

(21) Nichele, F.; Portolés, E.; Fornieri, A.; Whiticar, A. M.; Drachmann, A. C. C.; Gronin, S.; Wang, T.; Gardner, G. C.; Thomas, C.; Hatke, A. T.; Manfra, M. J.; Marcus, C. M. Relating Andreev Bound States and Supercurrents in Hybrid Josephson Junctions. *Phys. Rev. Lett.* **2020**, *124*, 226801.

(22) Lefevre-Seguin, V.; Turlot, E.; Urbina, C.; Esteve, D.; Devoret, M. H. Thermal activation of a hysteretic dc superconducting quantum interference device from its different zero-voltage states. *Phys. Rev. B* **1992**, *46*, 5507.

(23) Indolese, D. I.; Karnatak, P.; Kononov, A.; Delagrange, R.; Haller, R.; Wang, L.; Makk, P.; Watanabe, K.; Taniguchi, T.; Schönenberger, C. Compact SQUID realized in a double-layer graphene heterostructure. *Nano Lett.* **2020**, *20*, 7129.

(24) Li, P.; Wen, Y.; He, X.; Zhang, Q.; Xia, C.; Yu, Z.-M.; Yang, S. A.; Zhu, Z.; Alshareef, H. N.; Zhang, X.-X. Evidence for topological type-II Weyl semimetal WTe_2. *Nat. Commun.* **2017**, *8*, 1.

(25) Murphy, A.; Bezryadin, A. Asymmetric nanowire SQUID: Linear current-phase relation, stochastic switching and symmetries. *Phys. Rev. B* **2017**, *96*, 094507.

(26) Friedrich, F.; Winkel, P.; Borisov, K.; Seeger, H.; Sürgers, C.; Pop, I. M.; Wernsdorfer, W. Onset of phase diffusion in high kinetic inductance granular aluminum micro-SQUIDs. *Supercond. Sci. Technol.* **2019**, *32*, 125008.

(27) Hazra, D.; Kirtley, J. R.; Hasselbach, K. Nano-superconducting quantum interference devices with suspended junctions. *Appl. Phys. Lett.* **2014**, *104*, 152603.

(28) Dausy, H.; Nulens, L.; Raes, B.; Van Bael, M. J.; Van de Vondel, J. Impact of Kinetic Inductance on the Critical-Current Oscillations of Nanobridge SQUIDs. *Physical Review Applied* **2021**, *16*, 024013.

(29) Tinkham, M. *Introduction to Superconductivity*, 2nd ed.; Dover Publications: 2004.

(30) Bagwell, P. F. Suppression of the Josephson current through a narrow, mesoscopic, semiconductor channel by a single impurity. *Phys. Rev. B* **1992**, *46*, 12573.

(31) Faucher, M.; Fournier, T.; Pannetier, B.; Thirion, C.; Wernsdorfer, W.; Villegier, J.; Bouchiat, V. Niobium and niobium nitride SQUIDs based on anodized nanobridges made with an atomic force microscope. *Physica C: Superconductivity* **2002**, *368*, 211.

(32) Shatz, L. F.; Christensen, C. W. Numerical inductance calculations based on first principles. *PloS one* **2014**, *9*, No. e111643.

(33) Annunziata, A. J.; Santavicca, D. F.; Frunzio, L.; Catelani, G.; Rooks, M. J.; Frydman, A.; Prober, D. E. Tunable superconducting nanoinductors. *Nanotechnology* **2010**, *21*, 445202.

(34) Sinko, M. R.; de la Barrera, S. C.; Lanes, O.; Watanabe, K.; Taniguchi, T.; Tan, S.; Pekker, D.; Hatridge, M.; Hunt, B. M. Superconducting contact and quantum interference between two-dimensional van der Waals and three-dimensional conventional superconductors. *Phys. Rev. Materials* **2021**, *5*, 014001.

(35) Hopkins, D. S.; Pekker, D.; Goldbart, P. M.; Bezryadin, A. Quantum interference device made by DNA templating of superconducting nanowires. *Science* **2005**, *308*, 1762.

(36) Niepce, D.; Burnett, J.; Bylander, J. High kinetic inductance NbN nanowire superinductors. *Physical Review Applied* **2019**, *11*, 044014.

(37) Endres, M. Data for Current-phase relation of a WTe2 Josephson junction. *Zenodo repository*, 2023. DOI: 10.5281/zenodo.7327662 accessed 28/04/2023.